Pulse Magnetic Properties Measurement and Characterization of Fe-Based Nanocrystalline Cores for High-Voltage Pulse Magnetics Applications

Yi Liu, *Member, IEEE*, Yibo Han, Siwei Liu, and Fuchang Lin, *Member, IEEE*

***Abstract*—Fe-based nanocrystalline (FE-N) cores are widely used in power electronics and pulsed power applications. In pulsed power applications, it always requires high excitation current (up to tens of kiloampere) to excite large-volume cores (up to hundreds of cubic centimeter) with fewer number of winding turns, and it is hard to use the traditional test scheme to obtain the pulse magnetic properties in this case. The principles and scopes for the application of pulse magnetic properties measurement circuits, including the single-winding test circuit and double-winding test circuit, are analyzed and presented. Although the double-winding test circuit is classical to test the hysteresis loop, the single-winding test circuit is not totally useless in some cases. Based on the double-winding test circuit, the initial magnetization curves and maximum hysteresis loops of toroidal FE-N cores with high and low remanence are obtained under a relative constant magnetization rate with the order of 0.7–7 T/μs, and an equivalent frequency from 49 to 650 kHz. The unsaturated permeability is calculated based on the experimental results and fitted with the magnetization rate. The loss densities and permeability are fitted and compared. A design procedure of the saturable pulse transformer is illustrated for the application of the testing results. It is proved that the initial energy loss and unsaturated permeability are used for the design of the pulse transformer, and the traditional core loss is suitable for the estimation of power loss under the repetitive operation condition.**

***Index Terms*—Fe-based nanocrystalline (FE-N), hysteresis, loss density, magnetic curve measurement, magnetic loss, magnetization curve, pulsed magnetic.**

I. INTRODUCTION

WITH the development of pulsed power technology in civilian and industrial applications, the requirements of pulse magnetic components, including pulse transformers, magnetic switches (MSs), magnetic core inductors, and magnetic core impulse current transformers, etc., are growing quickly [1]–[5]. Recently, due to their high repetition rate, high stability, and longevity, the pulse transformers and MSs are widely used in repetitive pulsed power sources for water treatment, decomposition of hazardous gases, food processing, and plasma production, etc., [1], [2], [6], [7]. Magnetic core inductors and impulse current transformers are also widely used in pulsed power sources for pulse shaping and pulse monitoring, respectively. Unlike the working modes of the magnetic components in power converters, the magnetic cores in pulse magnetic components are always magnetized under very high magnetization rates [7]–[11]. The magnetization rate is often larger than 1 T/μs, and sometimes over 50 T/μs in some applications. The practical repetition frequency of the pulse magnetic component is not very high, from tens of hertz to several kilohertz. But the equivalent frequency under a single pulse is very high, up to the orders of megahertz. Therefore, the working mode of magnetic pulse components has two features: High magnetization rate and high equivalent working frequency. However, the datasheets of the permeability and core loss provided by the manufacturers are generally obtained under 50-Hz sine wave excitations, and cannot be applied in power electronic and pulsed power design directly. It is necessary to pay attention to evaluate the magnetic properties of the magnetic core under pulse excitation, especially for high density and high-frequency pulsed power source design [6]–[8], [10].

Several past and recent studies have investigated the loss density and permeability of nanocrystalline cores and other magnetic cores, such as Ferrites, amorphous metal alloys, etc., [7], [9], [12], [13]. Fe-based nanocrystalline (FE-N), which has properties like high saturation flux, low or high remanence, high permeability, and low loss density, is often chosen as the material of the transformer core, MS, and filtering inductor, etc., [7], [9], [11], [14]–[17]. FE-N has specific applications for its different remanence. For example, FE-N with high remanence is thought to be good as the material of a MS in magnetic pulse compression. Normally, the coercive force of general magnetic material increases as the B_r/B_s increases (B_r is the remanence, and B_s is the saturated induction). However, the coercive force of FE-N decreases as the B_r/B_s increases, and it also has some effect on the loss densities of FE-N with different remanences. It is flexible to obtain high or low remanence FE-N by longitudinal magnetic processing or transverse magnetic processing, respectively. So it is necessary to focus on the pulse magnetic properties of FE-N with different remanences, and choose the suitable FE-N cores according to the specific application.

Currently, the pulse magnetic properties of FE-N cores under high magnetization rate are measured in the same or similar operating conditions [7], [11]. The methods can be divided into two categories. One is based on the MSs, and the pulse magnetic properties are obtained under the cosine pulse excitation

Manuscript received June 30, 2014; revised September 27, 2014 and November 13, 2014; accepted December 20, 2014. Date of publication December 30, 2014; date of current version August 21, 2015. This work was supported by the Independent Innovation Fund, Huazhong University of Science and Technology under Grant 2014QN221. Recommended for publication by Associate Editor K. Ngo.

The authors are with the State Key Laboratory of Advanced Electromagnetic Engineering and Technology, Huazhong University of Science and Technology, Wuhan 430074, China (e-mail: yiliu@hust.edu.cn; 609097999@qq.com; 8683774@qq.com; fclin@mail.hust.edu.cn).

Color versions of one or more of the figures in this paper are available online at http://ieeexplore.ieee.org.

Digital Object Identifier 10.1109/TPEL.2014.2386916

[7], [8]. The other is based on pulse magnetic components with constant magnetization rate, and the pulse magnetic properties are measured under the square wave pulse excitation [10], [11]. The pulse magnetic properties are analyzed from the *B-H* curves, and the measuring principles of the methods are similar. However, the arrangements of the tested windings around the magnetic core are not the same. Double-winding test circuit is classical and widely used while testing the hysteresis loops of magnetic cores [9], [12], [13], [16]. However, in some cases, including analysis of magnetic properties [4], [10] and the design of MSs [5], [8], single-winding test circuit is also applied to test the *B-H* curve and loss characterization. The choice of the test circuit will ultimately influence the testing results. In the design-oriented modeling and simulation of power electronics and pulsed power systems, accurate and practical models of the magnetic components are of significant importance. The simulation models of magnetic components, including reluctance models, permeance models, inductance matrix models, T-circuit models, and gyrator-capacitor models, have been investigated [19], [20]. A general dynamic magnetic circuit model including iron saturation and losses is proposed [21]. Dynamic high-fidelity magnetic equivalent circuits are accurate and physics-based models of magnetic components, but even the reduced-order ones are of high complexity [22], [23].

The purpose herein is to propose a theoretical, experimental, and easily used analysis of circuit selection in the measurement of pulse magnetic properties, and presents a method to guide the design of pulse magnetic components based on the common experimental results. The principles and scopes for the application of pulse magnetic properties measurement circuits, including the single-winding test circuit and double-winding test circuit, are analyzed and presented. Based on the double-winding test circuit, the dynamic *B-H* curves of FE-N cores with high and low remanences are measured under different magnetization rates and equivalent working frequencies. Two definitions of loss densities, including the energy loss density in initial magnetization, and the traditional core loss density (CLD), are distinguished and used to evaluate the FE-N with different remanences. Based on the experimental results, the loss densities and permeability of the two FE-N types are presented and compared. The design procedure of a saturable pulse transformer (SPT) is illustrated for the application of the testing results. The testing results are also available for practical magnetic designs of MSs, iron-core Rogowski coil, and iron-core inductors, but not restricted to them.

II. MEASUREMENT OF PULSE MAGNETIC PROPERTIES

A. Circuit Analysis

Fig. 1 shows the single-winding test circuit for measuring pulse magnetization characteristics. It is based on the *LC* series ferromagnetic resonance, where *C* is the energy storage capacitor; and *L* is the nonlinear inductor. There is a winding with *N* turns wound on the tested core. *S* is the discharge control switch, and R_s is the stray resistor of the resonant circuit, including the conductor resistor and equivalent resistor of core loss. Generally, according to $H_Q l = NI$, where H_Q is the demagnetization field, *l* is the mean magnetic path length, *N* is the number of turns, *I* is the demagnetization current, if the demagnetization field H_{Q} satisfies $H_Q > (1-2)H_c$, the core can be demagnetized effectively, where H_c is the coercive force [18]. The voltage across the magnetic core *u* is measured by a Tektronix P6015A (20-kV dc/40 kV peak (100 ms pulse width), bandwidth: 75 MHz, 1000×, 3 pF, 100 MΩ). The current *i* flowing through the winding is measured by a Pearson CT (Model: 110A. 0.1 V/A, maximum peak current: 10 kA, useable rise time: 20 ns, 3 dB pt. high: 20 MHz).

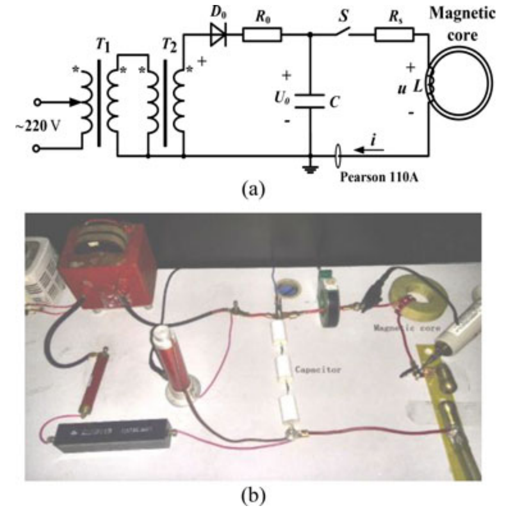

Fig. 1. Single-winding test circuit for measuring pulse magnetization characteristics. (a) Circuit schematic. (b) Picture of single-winding test circuit.

The magnetic induction *B* and average magnetic field intensity *H* are expressed as

$$B = \int_0^t u(t)\mathrm{d}t/(\eta N A) \tag{1}$$

$$H = N i(t) \ln(r_0/r_i)/2\pi(r_0 - r_i) \tag{2}$$

where, *N* is the number of turns; *A* is the cross-sectional area of the core; r_i and r_0 are the inner radius and the outer radius of the core, respectively; and η is the packing factor. The pulse magnetic properties of the magnetic core can be represented by the performance of the nonlinear inductor *L*. So the pulse magnetization process of the magnetic core can be described by *u*(*t*) and *i*(*t*). In the following analysis, the parasitic parallel capacitance and copper loss of the inductor are ignored. The performance of the nonlinear inductor *L* can be expressed by the Ψ-*i* characteristic, which is actually the reflection of the *B-H* curve in the circuit. The tested cores are well-demagnetized, and only the initial magnetization process is involved in the circuit analysis. As shown in Fig. 2, a piecewise linear approximation is used to estimate the initial magnetization curve, and the Ψ–*i* curve can be expressed as

$$\psi = \begin{cases} k_1 i, & (0 \le i \le i_1) \\ k_2 i + a, & (i_1 < i \le i_2) \\ k_3 i + b, & (i \ge i_2) \end{cases} \tag{3}$$

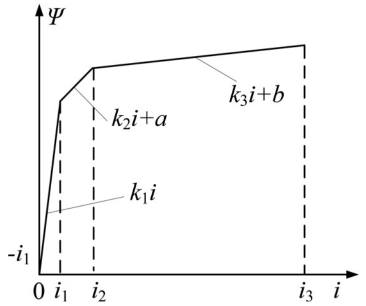

Fig. 2. Ψ–*i* characteristics of the initial magnetization process.

where Ψ is the magnetic flux, *i* is the current flowing through the winding, and *a* and *b* are constants. As shown in Fig. 2, in the interval $0 - t_1$, the core is unsaturated during magnetization process, and the permeability is high. The nonlinear inductor represents a large value of L_1. In the interval $t_1 - t_2$, the core is reaching the saturation stage. In this stage, the magnetic induction intensity *B* changes slowly with the magnetic field intensity *H*. The permeability decreases, and the nonlinear inductor represents a lower value of L_2. In the interval $t_2 - t_3$, the core is in the saturation stage. The magnetic permeability decreases to the minimum value, and the nonlinear inductor represents the average saturated inductance with the value of L_3.

When $0 < t \leq t_1$, according to the *LC* series resonance characteristics, it can be obtained that

$$i(t) = I_1 e^{-\alpha t} \sin \omega_1 t \tag{4}$$

where $I_1 = U_0 C/(L_1 C - 0.25 R_s^2 C^2)^{1/2}$, $\omega_1 = [1/(L_1 C) - 0.25 R_s^2 / L_1^2]^{1/2}$, and $\alpha = -0.5 R_s / L_1$.

While ignoring the copper loss of the testing circuit, there is $R_s = 0$. Then the voltage across the winding can be deduced as

$$u\left(t\right) = \begin{cases} k_1 \omega_1 I_1 \cos \omega_1 t, & (0 \leq t < t_1) \\ k_2 \omega_2 I_2 \cos\left[\omega_2\left(t - t_1\right) + \varphi\right], & (t_1 \leq t < t_2) \\ k_3 \omega_3 I_3 \cos\left[\omega_3\left(t - t_2\right) + \gamma\right], & (t_2 \leq t \leq t_3) \end{cases} \tag{5}$$

where

$$\begin{cases} U_1 = U_0 \cos \omega_1 t_1 \\ I_2 = \left(U_1^2 C / L_2 + i_1^2\right)^{1/2} \\ \omega_2 = \left(L_2 C\right)^{-1/2} \\ \varphi = \arcsin\left(i_1 / I_2\right) \end{cases} \tag{6}$$

$$\begin{cases} U_2 = U_1 \cos \omega_1 \left(t_2 - t_1\right) \\ I_3 = \left(U_2^2 C / L_3 + i_2^2\right)^{1/2} \\ \omega_3 = \left(L_3 C\right)^{-1/2} \\ \varphi = \arcsin\left(i_2 / I_3\right) \end{cases} \tag{7}$$

and the excitation current can be presented as

$$i\left(t\right) = \begin{cases} I_1 \sin \omega_1 t, & (0 \leq t < t_1) \\ I_2 \sin\left[\omega_2\left(t - t_1\right) + \varphi\right], & (t_1 \leq t < t_2) \\ I_3 \sin\left[\omega_3\left(t - t_2\right) + \gamma\right], & (t_2 \leq t < t_3) \end{cases} . \tag{8}$$

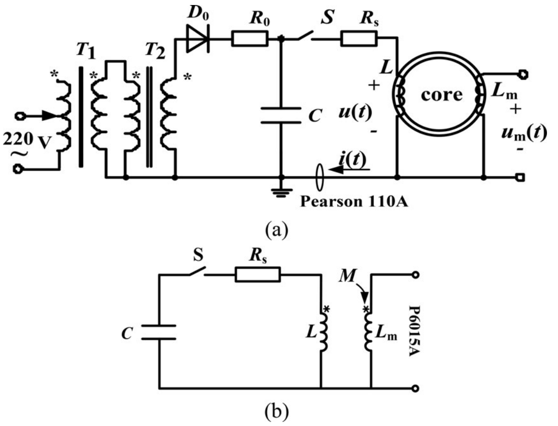

Fig. 3. Double-winding test circuit for measuring pulse magnetization characteristics. (a) Test stand. (b) Simplified circuit.

Fig. 3 shows the double-winding test circuit for measuring pulse magnetization characteristics. There is another test winding around the core with a certain number of turns compared to the single-winding test circuit. The measured electric parameters include the voltage across the secondary winding, and the excitation current through the primary winding. The two windings are coupled through the mutual inductance, and the simplified *LC* resonance circuit can be shown in Fig. 3(b). The current through the secondary winding is in the orders of microampere because of the high impedance of the voltage probe P6015A, and the current through the primary winding is in the range of several kiloampere. It can be thought that the secondary winding is open circuit, and the mutual inductance from the secondary winding to the primary winding is $M_{\mathrm{e-m}} = 0$. The secondary winding has no effect on the resonance circuit, so the voltage and excitation current can be calculated by (5) to (8). u_{m} is the open-circuit voltage across the secondary winding, and it has nothing to do with the self-inductance of the secondary winding. From the standpoint of the electric circuit, u_{m} is determined by the excitation current *i*(*t*) and the mutual inductance $M_{\mathrm{m-e}}$ from the primary winding to the secondary winding, and from the standpoint of the magnetic circuit, u_{m} is determined by the change of the magnetic induction intensity in the magnetic core. When the turns number satisfies $N_{\mathrm{s}} = N$, there is

$$u_m(t) = k_c u(t) \tag{9}$$

where k_c is the coupling coefficient, and $k_{ci} = M_{m-ei}/L_i (i = 1, 2, 3)$. The voltage across the primary winding can be deduced as

$$u\left(t\right) = \begin{cases} k_1 k_{c1} \omega_1 I_1 \cos \omega_1 t, & (0 \leq t < t_1) \\ k_2 k_{c2} \omega_2 I_2 \cos\left[\omega_2\left(t - t_1\right) + \varphi\right], & (t_1 \leq t < t_2) \\ k_3 k_{c3} \omega_3 I_3 \cos\left[\omega_3\left(t - t_2\right) + \gamma\right], & (t_2 \leq t \leq t_3) \end{cases} . \tag{10}$$

In the initial magnetization process, $u_{\mathrm{m}}(t)$ is composed of three sections of continuous cosine waveforms with attenuated amplitude and increased frequency. There is $k_{c1} > 0.95$ before the core saturation, and $k_{c3} \rightarrow 0$ after the core saturation. In the interval $t_2 < t \leq t_3$, there is $u_{\mathrm{m}}(t) < u(t)$.

B. Calibration of Time Delays of the Probes

Some measures are taken to improve the accuracy and resolution of the magnetization curve during the test. The delay time of P6015A with 10 ft cable is only 14.7 ns, in which the transmission time in the cable contributed 12.4 ns. Besides, the phase shift of CT110A is below to 1% in its bandwidth. That is to say, the delay times in the transmission cables contribute most of the time delay difference between P6015A and CT110A, so the cables with the same length are applied to reduce the time delay difference. Necessary calibration experiments are conducted to testify the time delay. To construct a calibration circuit, the iron-core inductor in Fig. 1 is replaced by an air-core inductor, whose inductance is below to 10 μH. P6015A and CT110A are used to measure the voltage across the inductor u_{ca} and the current through the inductor i_{ca}, respectively. The resistance of the air-core inductor is several milliohm at 10 Hz–1000 kHz, and the parasitic parallel capacitance is typically a few picofarad [24]. Consequently, the inductor can be seen as a pure inductance, and the voltage waveforms obtained by P6015A shall be 90° ahead of the current waveforms obtained by CT110A. Several typical waveforms under different calibration frequencies f_{ca} are shown in Fig. 4. The time delay difference between P6015A and CT110A is always less than one sampling interval from 42 to 659 kHz. The voltage and current offset are set zero on computer. It is accepted by the experimental results.

C. Errors Estimation

Possible errors in the test are discussed as follows.

1) *Error Caused by Time Delay Difference:* When the signal of CT110A is transmitted slower than that of P6015A, the unsaturated section of initial *B-H* curve will be steeper; otherwise, it will be flatter. According to the calibration, the delay difference is less than one sampling interval. The sampling points of oscilloscope TDS2024B is 10 000, then the error caused by time delay difference varies with the sampling length. Namely, the higher the frequencies of voltage and current are, the better accuracy the test has.
2) *Error Caused by Circuit Parasitic Parameters:* When the parasitic parallel capacitance is a few picofarad, the FE-N core inductor can still be seen as a pure inductance. Small parasitic parallel capacitance may cause unwanted resonance above megahertz. The superposition oscillation always lasts less than 100 ns after closing *S*, and the magnitude is often less than 10% of the real magnitude of *u*. Besides, the integration of *u* reduces the error caused by the oscillation.
3) *Error Caused by Offset Compensation:* The offsets are compensated from dozens volts or amperes to less than 0.1 V or ampere by deducting the average of data before $t = 0$. Consequently, the corresponding error can be ignored.

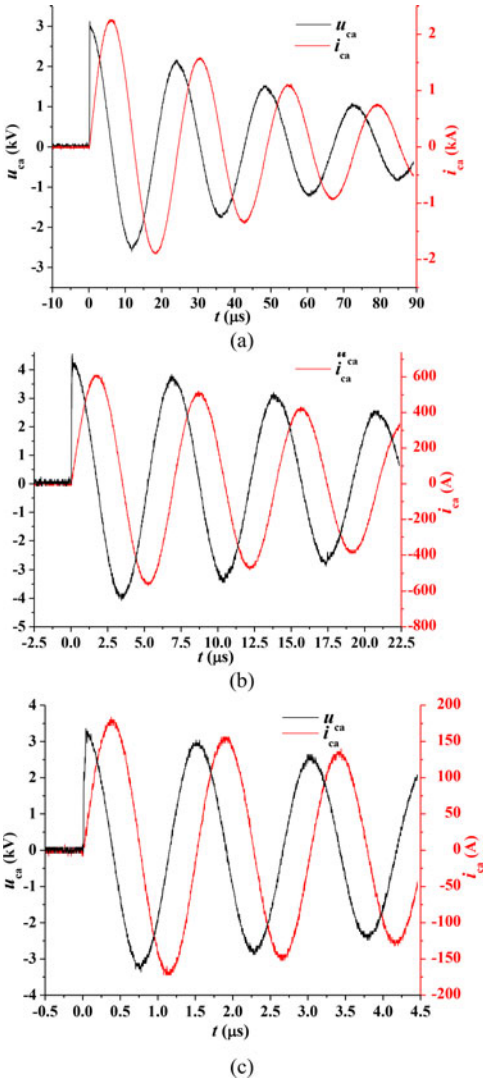

Fig. 4. Waveforms of $u_{ca}(t)$ and $i_{ca}(t)$ under different frequency. (a) $f_{ca} = 42$ kHz; (b) $f_{ca} = 146$ kHz; and (c) $f_{ca} = 659$ kHz.

TABLE I
DATASHEETS OF FE-N CORES WITH LOW AND HIGH REMANENCE

Remanence		Low	High
At 50 Hz	B_{s} (T)	1.0	1.0
	$B_{\mathrm{r}}/B_{\mathrm{s}}$	0.25	0.85
	H_{c} (A/m)	2.5	5.0
Loss density (W/kg) (0.5T/20kHz)		32	74
Material		1K107	1K107
Magnetic field annealing		Transverse	Longitudinal
Lamination thickness (μm)		30	30

D. Experimental Results

A single-winding test circuit is constructed according to Fig. 1, where $C = 75$ nF, $U_0 = 5.5$ kV, and $N = 3$. A FE-N core with outer diameter of 110 mm, inner diameter of 60 mm, height of 20 mm, and packing factor of 0.8 was tested (the material will be introduced in Table I). The typical measured voltage *u*(*t*) and current *i*(*t*) are shown in Fig. 5. A digital filter program based on Savitzky–Golay algorithm is used to smooth the waveforms. The original and the processed waveforms are shown in Fig. 10. (Black line is the original, and the red line is

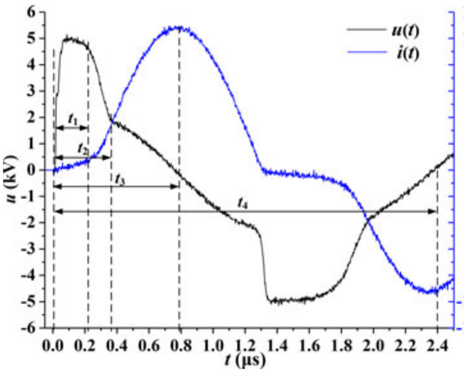

Fig. 5. Typical waveforms of *u*(*t*) and *i*(*t*) under the single-winding test with $\mathrm{d}B/\mathrm{d}t = 3.7$ T/μs.

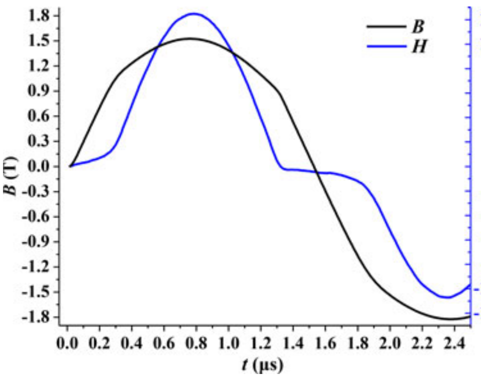

Fig. 6. Waveforms of *B*(*t*) and *H*(*t*) under the single-winding test with $dB/dt = 3.7$ T/μs.

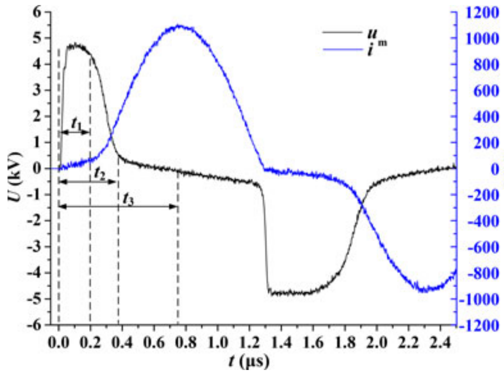

Fig. 7. Typical waveforms of *u*(*t*) and *i*(*t*) under the double-winding test with $dB/dt = 3.7$ T/μs.

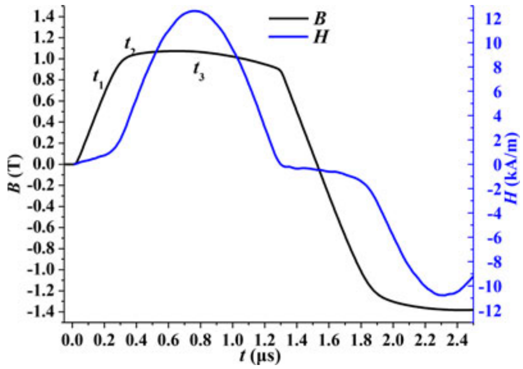

Fig. 8. Waveforms of *B*(*t*) and *H*(*t*) under the double-winding test with $dB/dt = 3.7$ T/μs.

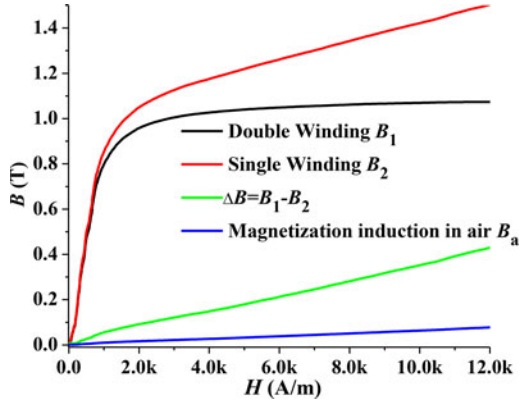

Fig. 9. Initial magnetization curves and space magnetization characteristics.

that after processed.) It just smoothed the waveform, and does not change the shape. *B*(*t*) and *H*(*t*) can be obtained from (1) and (2). The interval $0 - t_3$ represents the initial magnetization process, and the oscillation waveform after t_3 corresponds to the reverse magnetization process under a certain frequency.

As shown in Figs. 5 and 6, the waveform of *u*(*t*) is consistent with the three stages analyzed in Section II. If only considering two magnetization stages from the unsaturation to saturation process, it will not be in conformity with the experimental phenomena. It can be concluded that the becoming saturated process is prominently in the pulse magnetization process of the FE-N core. In the interval $0 - t_1$, the waveform of *u*(*t*) can be approximate to a square wave with a small amplitude attenuation, and *B* rises linearly when the magnetization rate is $dB/dt = 3.7$ T/μs. In the interval $t_1 - t_3$, the waveform of *B*(*t*) can be thought to the sine function wave.

A double-winding test circuit is constructed according to Fig. 3. The parameters are the same with Fig. 1, and there is $N_\mathrm{m} = N = 3$. The typical measured $u_\mathrm{m}(t)$ and *i*(*t*) are shown in Fig. 7. From the experimental results, it can be obtained that the coupling coefficient k_{c1} is 0.96 before the core saturation, and k_{c2} is less than 0.1 after the core saturation. The corresponding *B*(*t*) and *H*(*t*) are shown in Fig. 8. In the interval $0 - t_1$, *B* rises linearly when the magnetization rate is $dB/dt = 3.7$ T/μs. In the interval $t_1 - t_3$, the waveform of *B*(*t*) can be thought to the sine function wave. However, the amplitude does not have a significant growth due to $k_{c3} < 0.1$.

E. Analysis and Discussion

The initial magnetization curve can be obtained from Figs. 6 and 8. As shown in Fig. 9, the initial magnetization curves obtained by the single-winding test and double-winding test are shown as B_1 and B_2, respectively. The difference between the two initial magnetization curves is presented as ΔB, and the space magnetization curve is shown as B_a. ΔB reflects the space magnetization characteristic of the magnetic core coil after the core saturation. In the single-winding test circuit, the winding inductance *L* can be thought to be consisted of a saturable inductance $L_{\rm c}$ by the effective core cross-sectional area ηA and a constant inductance L_a by the surrounded area A_w. The voltage across the inductance *L* can be expressed as

$$u = u_c + u_a \tag{11}$$

where $u_{\rm c}$ is the induced voltage caused by the changing of the magnetic induction intensity $B_{\rm c}$

$$u_c = \eta N A \frac{{\rm d}B_c}{{\rm d}t}. \tag{12}$$

For the single-winding test, equation (1) can be expressed as

$$B_{1r} = \frac{\int_0^t u_c(t)\,{\rm d}t}{\eta N A} + \frac{\int_0^t u_a(t)\,{\rm d}t}{N A_w}. \tag{13}$$

However, it is difficult to divide *u* into $u_{\rm c}$ and u_a. The magnetic induction intensity B_1 can be calculated by

$$B_1 = \frac{\int_0^t u(t)\,{\rm d}t}{\eta N A} = \frac{\int_0^t u_c(t)\,{\rm d}t}{\eta N A} + \frac{\int_0^t u_a(t)\,{\rm d}t}{\eta N A}. \tag{14}$$

For the double-winding test, ignoring the resistor and leakage flux of the winding, there is $u_{\rm m} \approx u_{\rm c}$, and

$$B_2 = \frac{\int_0^t u_c(t)\,{\rm d}t}{\eta N A}. \tag{15}$$

In Fig. 9, there is

$$\Delta B = B_1 - B_2 = \frac{\int_0^t u_a(t)\,{\rm d}t}{\eta N A}. \tag{16}$$

After the core saturated, the actual equivalent space magnetic induction intensity is

$$B_a = B_{1r} - B_2 = \frac{\int_0^t u_a(t)\,{\rm d}t}{N A_w}. \tag{17}$$

Combining (16) and (17), there is

$$B_a = \frac{\eta A}{A_w}\Delta B. \tag{18}$$

If the cross-sectional area of the winding is the same as the effective cross-sectional area of the magnetic core, the difference between the two initial magnetization curves under different test methods should be the space magnetization. However, the packing factor of FE-N core is always 0.7–0.8. The winding cannot be close to the core surface due to insulation consideration. The cross-sectional area of coil is always larger than the effective cross-sectional area of the magnetic core. The space magnetization effect is enlarged in the single-winding test circuit according to (18). But for the double-winding test, the coupling is mainly determined by the magnetic core, and the coupling becomes poor after the core saturated. The saturation characteristics of the magnetic material can be measured accurately in the double-winding test. The unsaturated and saturated permeability obtained from the initial magnetization curve are larger. In Fig. 9, when $H = 6$ kA/m, the relative saturated permeability from the initial magnetic curve in the single-winding test is $\mu_{\rm rs1} = 33.9$, and that in the double-winding test circuit is $\mu_{\rm rs2} = 5.85$. From the space magnetization curve, the relative saturation permeability is $\mu_{\rm rsa} = 5.94$ at $H = 6$ kA/m, and it is in agreement with the results of the double-winding test. The little difference is caused by the ignoring of the leakage magnetic flux. The effective cross-sectional area of FE-N core is determined by packing coefficient η. The effect of space magnetization on the experimental results after the core saturation is enlarged, and this error cannot be reduced through other measures. What's more, the exciting winding cannot be completely close to the insulation surface of the tested core. There is also a skin effect on the winding under high frequency. The difference of the effective cross sections A_w and A is caused by all the factors. There is an inherent error during the measurement under single-winding test circuit, and the winding should be considered close to the magnetic core shell as close as possible to reduce the error.

The voltage-second product (VSP) is one of the key parameters for the pulse magnetic component design. The VSP obtained in the two test methods will not be the same because of the effect of space magnetization. The VSP from the single-winding test represents the saturation characteristics of the nonlinear inductor, and that from the double-winding test represents the saturation characteristics of the magnetic core. Considering the definition of VSP, the VSP obtained from the single-winding circuit should be redefined as the apparent voltage-second product (AVSP) of the magnetic core, or the VSP of the nonlinear inductor, and that from the double-winding circuit is the VSP of the magnetic core. The VSP can be measured by

$$VSP = \int_0^{t_s} u(t){\rm d}t \tag{19}$$

$$VSP = \Delta B N \eta A. \tag{20}$$

In engineering, the VSP is usually obtained under a certain induction incremental Δ*B* for a specific magnetic core. The core gets saturated after t_2. Based on the measured *u*(*t*) and $u_{\rm m}(t)$, it can be deduced that the AVSP in the single-winding circuit is 1.48 kV·μs, and the VSP from the double-winding circuit is 1.25 kV·μs. AVSP is much more appropriate to be used in the design and analysis of pulse magnetic components with a single winding, such as MSs, and magnetic core pulse inductors. VSP is suitable for the design of pulse magnetic components with double windings, such as pulse transformers, and magnetic core pulse current transformers.

In the single-winding test, it can be concluded that the magnetic properties of the FE-N after the core saturation cannot be reflected accurately due to the packing factor of the FE-N core and the winding construction of pulsed magnetic components. But it is useful in some cases. For example, Ψ–*i* curve is important for the simulation and analysis of MS in pulsed power technology and iron-core reactors in power systems. In these cases, Ψ–*i* curve shall be obtained by testing voltage and current waveforms in single-winding circuits because air magnetization is included in the characteristics after saturation. In this case, additional series saturation inductance is excess, and the winding must be constructed the same as the actual situation.

However, when testing the *B*-*H* curve of magnetic core for further analysis of magnetic properties, the double-winding circuit will be a better choice. Besides, both circuits can be used for the design of pulsed power magnetic components. The winding pattern of the testing circuit had better be the same as the component in design. As for the determination of average saturation inductance, different calculation method shall be used.

From the insight of loss, if ignoring the copper loss, the loss densities (including energy loss during initial magnetization and traditional core loss) obtained by the single-winding test contain the part of leakage magnetic loss in air. Consequently, the double-winding test will be better for the evaluation of the loss characteristic of cores, and the single-winding test is preferred for the loss test of actual magnetic component.

III. CHARACTERIZATION OF FE-N CORES

Based on the double-winding test circuit, the FE-N cores with high and low remanence are tested. The datasheet of cores under test is shown in Table I. Both the two types of cores have the same dimensions: Outer radius $r_o = 55$ mm, inner radius $r_i = 30$ mm, and height $h = 20$ mm. The packing coefficient is 0.8. Normally, the saturation induction of FE-N is about 1.2 T. As better for pulsed power applications, the saturation flux of the cores is sacrificed a little for the improvement of other properties by doping and annealing processes to some extent. The remanences of the two types of FE-N cores are 0.25 and 0.85 T, respectively. A circuit producing $I = 0.5$ A alternating current with $N = 5$, $H_Q = 6.6\ \mathrm{A/m} > (1-2)H_\mathrm{c}$ is used to demagnetize the core to the initial point ($H = 0\mathrm{A/m}, B = 0T$) prior to each shot. The alternating current lasts for 1 min and then goes to zero gradually.

The typical waveforms are shown in Fig. 10. The current waveform smoothed by the Savitzky–Golay algorithm is shown as the red line.

The voltage across the tested core is similar to a square pulse, and the magnetization rate can be considered to be constant and calculated by

$$\frac{\mathrm{d}B}{\mathrm{d}t} = \frac{U}{N_t A} \tag{21}$$

where *U* is the voltage across the tested core measured in the test stand; N_t is the number of turns; and *A* is the effective cross-sectional area of the core. The corresponding *B*–*H* curve can be derived based on (3) and (4). The *B*–*H* curves based on filtered and unfiltered current waveforms are shown in Fig. 10(b).

During the measurement, the capacitance and charging voltage is selected to keep the consistent maximum magnetic field intensity. The peak value of the excitation current is 1 kA, and it corresponds to the maximum magnetic field intensity of 10 kA/m. The initial magnetization curves under different magnetization rates and hysteresis loops under different equivalent frequencies are obtained under different capacitances and charging voltages. The test parameters of FE-N cores with low and high remanences are shown in Table II.

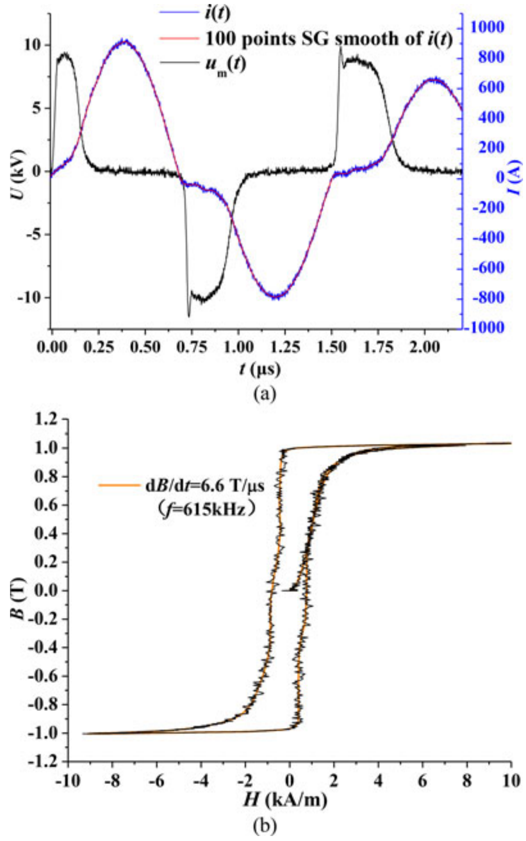

Fig. 10. (a) Typical voltage and current waveforms at 6.6 T/μs (equivalent frequency of 615 kHz); (b) Initial curve and hysteresis loop based on the data in (a). (Yellow line represents the smoothed curve).

TABLE II
TEST PARAMETERS OF FE-N CORES

Parameters	Low remanence			High remanence		
C(nF)	U_0 (kV)	d*B*/d*t* (T/μs)	*f*(kHz)	U_0 (kV)	d*B*/d*t* (T/μs)	*f*(kHz)
2500	0.93	0.7	49	0.92	0.7	49
300	3	2.1	151	3	2.1	151
150	4	2.7	208	4	2.6	208
75	5	3.7	303	6	3.8	303
50	10	5.2	363	7.5	4.7	361
25	11	5.6	504	11	5.6	506
15	14.2	7.1	650	14	6.6	615

A. Initial Magnetization Characteristics

As shown in Fig. 11, the initial magnetization *B*–*H* curves of low- and high-remanence FE-N cores under different d*B*/d*t* from 0.7 to 7.0 T/μs are obtained and presented. As shown in Fig. 11, the maximum magnetic field intensity reaches $H_{\max} = 6$ kA/m. Actually, the FE-N material completely saturates to a relative permeability of unity at a large magnetic field (more than 10^4 A/m) [1]. It is not considered in this paper. When magnetic field *H* reaches 6 kA/m approximately, the saturation fluxes B_s of the FE-N are 1.0 T. As the magnetization rate increases, due to the influence of magnetic viscosity and eddy current, the

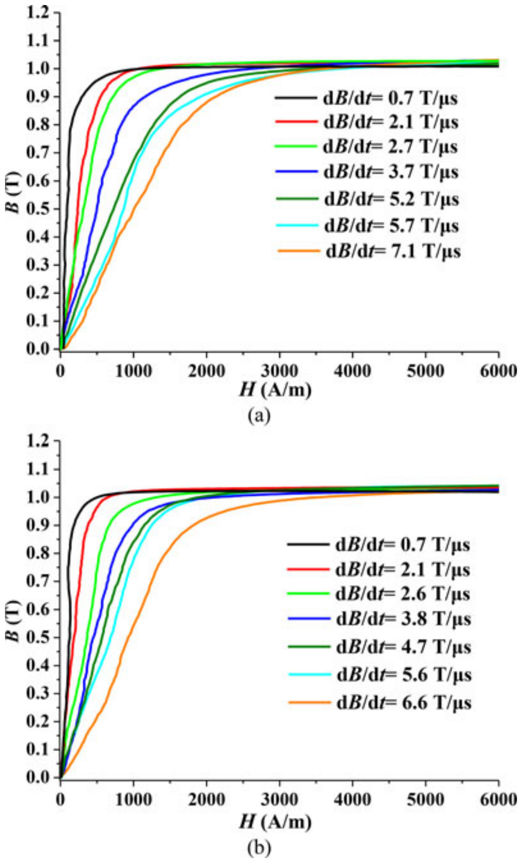

Fig. 11. Initial magnetization curves of *B*-*H* curves. (a) Low remanence FE-N; (b) high remanence FE-N.

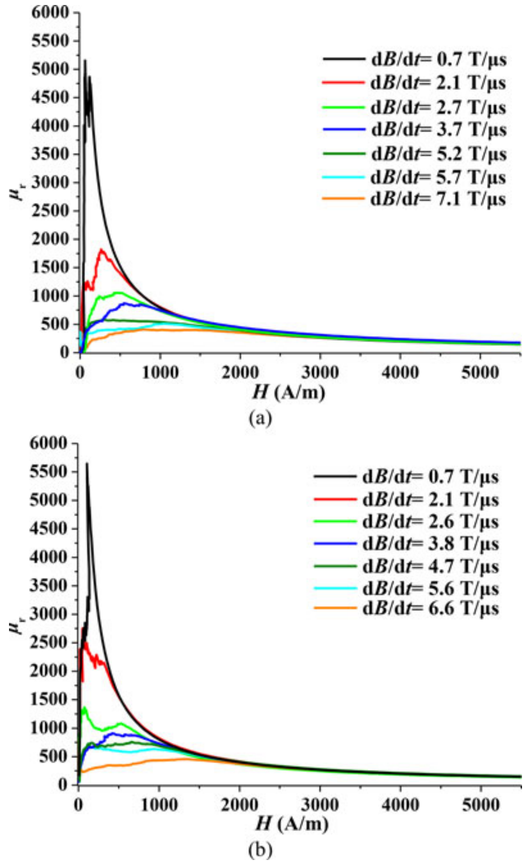

Fig. 12. Relative permeability curves under different d*B*/d*t*. (a) Low remanence FE-N; (b) high remanence FE-N.

magnetization curve rises slowly. The relative permeability of FE-N versus the magnetic field is shown in Fig. 12. The relative permeability is obtained from the initial magnetization curves shown in Fig. 12 using [18]

$$\mu = \frac{B}{\mu_0 H} \tag{22}$$

where μ_0 is the vacuum permeability; and μ is the relative permeability of the core material. Under a certain magnetization rate, as the magnetic field intensity increases, the relative permeability increases rapidly first, and then declines slowly. When the magnetization rate is lower than 2.7 T/μs, there are two peak values on the relative permeability curve. The relative permeability reaches its first peak value when the magnetic field is less than 100 A/m. When 2.1 T/μs ≤ d*B*/d*t* ≤ 3.7 T/μs, the peak value of relative permeability corresponds to the magnetic field intensity of 300–600 A/m. For the curve under $dB/dt = 2.1$ T/μs, the maximum value of the relative permeability is located at the second peak. As the magnetization rate increases further, there is no longer a significant peak on the relative permeability curve, and the curve is changing more gently.

Fig. 13 shows the relationship between the maximum relative permeability and d*B*/d*t*, *H*. As d*B*/d*t* increases, the maximum relative permeability decreases. Under the same d*B*/d*t*, the maximum relative permeability of FE-N core with high remanence is larger than that of low remanence. When d*B*/d*t* is 2.7 T/μs, both the two types of cores have a turning point on the maximum relative permeability curve. The difference between the two types of cores is decreased as d*B*/d*t* increases. As shown in Fig. 13, the fitting equations of maximum relative permeability associated with magnetization rate can be expressed as, respectively

$$\mu_{\max 1} = \begin{cases} 6525.6 - 2102.7\dfrac{\mathrm{d}B}{\mathrm{d}t}, & \dfrac{\mathrm{d}B}{\mathrm{d}t} < 2.7\,\mathrm{T}/\mu\mathrm{s} \\ 1430.6 - 153.6\dfrac{\mathrm{d}B}{\mathrm{d}t}, & \dfrac{\mathrm{d}B}{\mathrm{d}t} > 2.7\,\mathrm{T}/\mu\mathrm{s} \end{cases} \tag{23}$$

$$\mu_{\max 2} = \begin{cases} 7215.5 - 2220.5\dfrac{\mathrm{d}B}{\mathrm{d}t}, & \dfrac{\mathrm{d}B}{\mathrm{d}t} < 2.7\,\mathrm{T}/\mu\mathrm{s} \\ 1795.7 - 209.1\dfrac{\mathrm{d}B}{\mathrm{d}t}, & \dfrac{\mathrm{d}B}{\mathrm{d}t} > 2.7\,\mathrm{T}/\mu\mathrm{s} \end{cases} \tag{24}$$

where $\mu_{\max 1}$ $\mu_{\max 2}$ are the maximum relative permeability of low-remanence and high-remanence FE-N cores, respectively. When d*B*/d*t* is lower than 4 T/μs, the value of the maximum relative permeability of FE-N with the high remanence is larger than that of the low remanence FE-N. Then the values of the maximum relative permeability are nearly the same under high magnetization rate.

The average relative permeability corresponding to different flux swing under different d*B*/d*t* is shown in Fig. 14. The values of average permeability were calculated in three situations (0.0–0.4 T, 0.4–1.0 T, and 0.0–0.8 T).The average permeability of the core can be obtained by

$$\mu_{\mathrm{av}} = \frac{\Delta B}{\mu_0 \Delta H} \tag{25}$$

where ΔB is the magnetic flux density, and ΔH is the magnetic field increment corresponding to ΔB. As the magnetization rate increases, the average relative permeability of the two FE-N types decreases. Under the same magnetization rate, the value of the average relative permeability of the low remanence FE-N is larger than that of the high remanence FE-N. But as the magnetization rate reaches 2.7 T/μs or higher, the difference between the average permeability of the two FE-N types is very small. Both to the two FE-N types, the average relative permeability corresponding to magnetic flux swing 0.4–1.0 T is not much higher than that corresponding to magnetic flux swing 0.0–0.4 T. It is found that there is not a so fast rising stage in the *B–H* curve under high magnetization rate because the *B–H* curve rises slowly and change gradually due to high magnetization rate.

B. Loss Characterization

Loss analysis is crucial for the design of magnetic components in high-voltage pulse applications. It should be clarified that there are two kinds of losses under pulse excitations. The traditional one is the heat dissipated during cyclical magnetization and demagnetization and calculated by the area of hysteresis loop. The other one is the energy loss needed to saturate a magnetic component, for MS, it is defined as switching loss [7]. In a simple pulsed power system like the two testing circuits in this paper, energy is usually stored in capacitors. With the switch closed, the energy will be released from the capacitor, and transferred to the magnetic energy temporarily stored in core and air, iron loss of the core, and copper loss of the loop. The magnetic energy makes it possible for magnetic components to increase the voltage or compress the pulse shape. The transformation process corresponds to the duration from $t = 0$ to $t = t_3$ in Fig. 5, which is also the interval of the initial magnetization process. The energy loss density can be calculated by (26) and shown in Fig. 15

$$\text{Initial Energy Loss Density (IELD)} = \int_0^{t_1} H dB = \sum_{i=0}^{j} \{H(i)[B(i) - B(i-1)]\} \tag{26}$$

where *j* is the point samples of the data in the initial magnetization curve.

The physical meaning of the energy density enclosed in the enclosed area by the initial *B–H* curve and the vertical *B*-axis varies with the testing circuit. If the single-winding test circuit is applied, as presented in [7] and [10], the area of "*B–H* curve" ($\mathrm{IELD_s}$) contains three parts: Magnetic energy temporarily stored in core and air, iron loss of the core, and copper loss of the winding. However, if the *B-H* curve is obtained from the double-winding test circuit, the effect of the air magnetization will be eliminated. Besides, the induced voltage across the secondary winding contributes no copper loss. Consequently, the area ($\mathrm{IELD_d}$) is only the summary of the magnetic energy temporarily stored in the core and the iron loss of the core. Evidently, $\mathrm{IELD_s}$ is dependent on the winding arrangement and circuit characteristic. It is actually the energy loss for a certain component with the certain condition. Initial energy loss (IEL) can be defined as the total energy that transfers to the core in the initial magnetization process. It contains two parts: First one is the magnetic energy temporarily stored in core, and the second one is the traditional iron loss. The first part of the IEL is temperately absorbed by the core and stored in the form of magnetic energy.

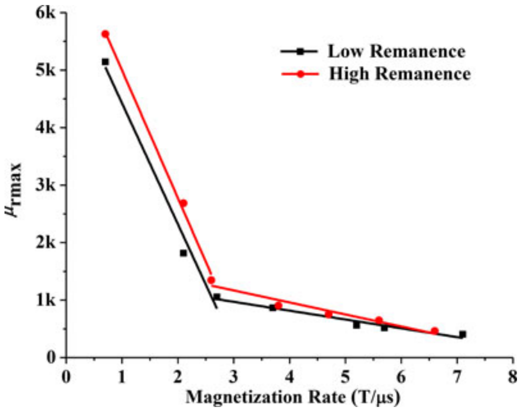

Fig. 13. Maximum relative permeability of FE-N core versus the magnetization rate.

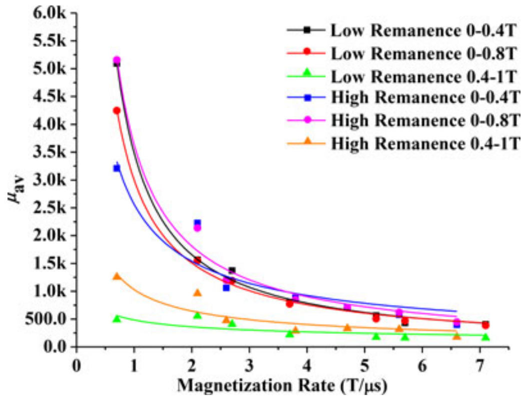

Fig. 14. Average relative pulse permeability versus the magnetization rate.

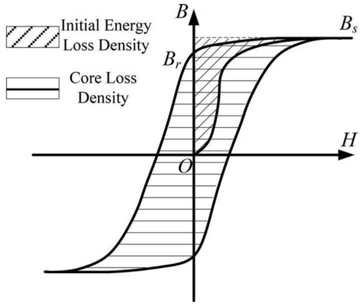

Fig. 15. IEL density and traditional CLD.

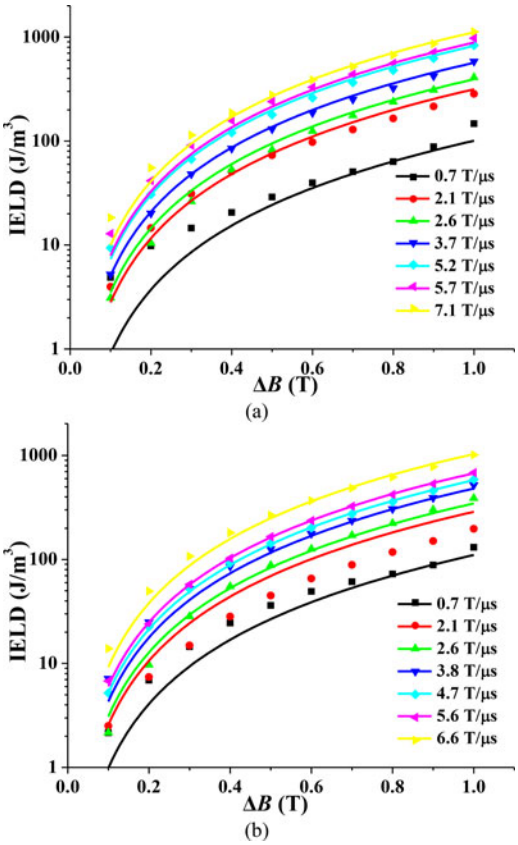

Fig. 16. Loss density of FE-N core versus the flux swing. (a) Low remanence FE-N; (b) high remanence FE-N.

It will be released in the following oscillation. The second part is dissipated in the form of heat. IELD can be thought to be the IEL of a core with a volume of 1 m^3 and can be calculated from the initial *B-H* curve as presented by (26). IELD obtained from the double-winding test circuit is the energy that the core needed to be saturated, no matter what component structure is, and how the circuit characteristic changes.

IELD increases slowly when the flux swing of the core is lower than 0.6 T. As the flux swing increases, IELD increases fast, especially under high magnetization rate. There is not a good microscopic physical magnetization model for the IELD calculation because the rather chaotic time and space distribution of the magnetization changes cannot be described exactly. According to specific applications, some available core loss calculation models based on macroscopic physical mechanisms are used to describe the losses, such as the loss separation approach and empirical equations [9], [10], [16], [17]. In this paper, it is tried to fit the loss densities. As shown in Fig. 16, the IELD fitting equation of the low and high remanence FE-N associated with magnetization rate and magnetic induction increment can be expressed as

$$\mathrm{IELD}_{\mathrm{Low}} = 145.9\left(\frac{\mathrm{d}B}{\mathrm{d}t}\right)^{1.04}\Delta B^{2.05} \tag{27}$$

$$\mathrm{IELD}_{\mathrm{High}} = 150.86\left(\frac{\mathrm{d}B}{\mathrm{d}t}\right)^{0.87}\Delta B^{2.05}. \tag{28}$$

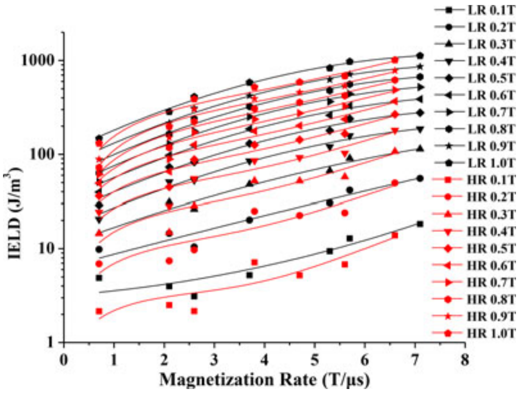

Fig. 17. IELD of FE-N cores versus the magnetization rates (LR: Low Remanence; HR: High Remanence).

It should be noted that the fitting equation (28) is valid only when d*B*/d*t*<6.6 T/μs. For high remanence FE-N, when d*B*/d*t* = 6.6 T/μs, the fitting equation of the IELD can be expressed as

$$\mathrm{IELD}_{\mathrm{High}(6.6\mathrm{T}/\mu s)} = 200.1\left(\frac{\mathrm{d}B}{\mathrm{d}t}\right)^{0.87}\Delta B^{2.05}. \tag{29}$$

It shows that the loss densities are proportional to the power functions of the magnetization rate and magnetic induction increment. The power index of the magnetic induction increment is close to 2. The IELD of the high remanence FE-N is much more related to the magnetic induction increment, and that of the low remanence FE-N is more sensitive to the change of magnetization rate.

Fig. 17 shows the IELD versus d*B*/d*t* in regard to different flux swing ΔB from the initial point ($H = 0$ A/m, $B = 0$ T) with an interval of 0.1 T. As shown in Fig. 17, both the FE-N cores with high and low remanences deliver lower IELD at the lower magnetization rates. Under each flux swing, the loss of the low-remanence FE-N core is a little higher than that of the high residual one. As the flux swing increases, the difference of the IELD between the two different FE-N cores gets larger and larger. When the flux swing is lower than 0.4 T, the FE-N cores with high and low remanence present low IELD and are less than 200 J/m^3. It can be concluded that the FE-N cores can work under high repetition when the flux swing is lower than 0.4 T.

High magnetization rates in FE-N alloys are associated with high magnetic losses due to induced eddy currents. Losses not only reduce efficiency, but also result in increases in core temperature, which ultimately limit the maximum frequency or repetition rate at which the core can be used. In pulsed power, high repetition rate is usually necessary for high average output power. The quantity of the magnetic material used in pulse transformer and inductor is related to the flux handling capabilities of the materials. This capability is determined by the product of the cross-sectional area of the core and the achievable change in flux density. As shown in Fig. 18, the hysteresis loops of low- and high-remanence FE-N cores under different equivalent frequencies from 49 to 650 kHz are obtained and presented. The equivalent frequency is defined based on the waveform of

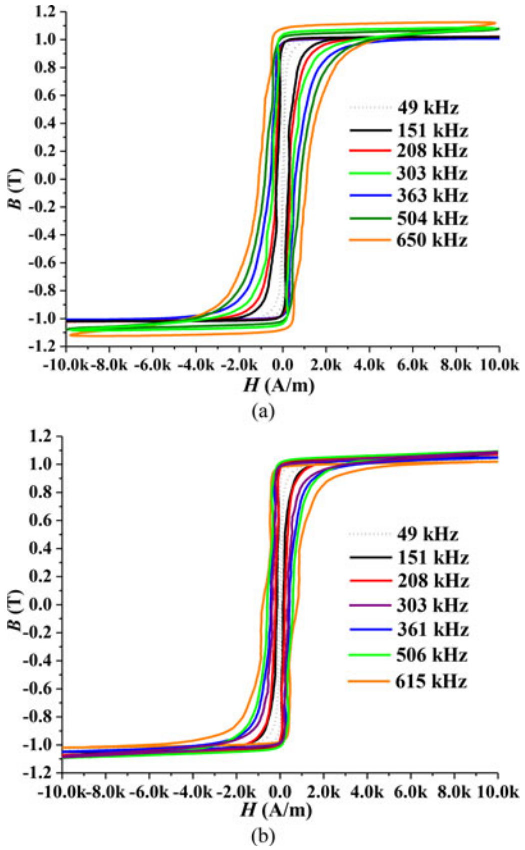

(a)

(b)

Fig. 18. Hysteresis loops of *B*–*H* curve. (a) Low remanence FE-N; (b) high remanence FE-N.

excitation current. In Fig. 5, t_3 and t_4 are the moments when the excitation current reaches its first and second peak, respectively, which are corresponding to the half cycle of the hysteresis loop from $+B_s$ to $-B_s$. Consequently, the equivalent frequency of the hysteresis loop is calculated by

$$f = \frac{1}{2(t_4 - t_3)}. \tag{30}$$

The loss densities per cycle are calculated based on the hysteresis loops, as shown in Fig. 19. The area of the hysteresis loop is the traditional loss density, and it can be written as CLD. The fitting equations of the loss densities can be expressed as, respectively

$$\mathrm{CLD}_{\mathrm{Low}} = 11.20\,f - 361.0 \tag{31}$$

$$\mathrm{CLD}_{\mathrm{high}} = 6.222\,f + 183.9. \tag{32}$$

It is noticed that the difference between all-cycle loss densities of the two cores are reducing with the decrease of *f*. Besides, according the datasheet in Table II, the loss density of the low-remanence core is lower than that of the high-remanence one at lower frequency. Additionally, for the FE-N, it is universally acknowledged that low-remanence core annealed under transverse magnetic field has lower loss density than that of the high-remanence core annealed under longitudinal magnetic field [25]. In this case, a conclusion can be deduced as follows. The loss density of the low-remanence core will not keep lower than that of the high-remanence one at all frequencies. The magnitude relationship between the loss densities of the low- and high-remanence FE-N cores may turn upside down at a rather high frequency (in this paper, the turning frequency is approximate 100 kHz). When the cores are worked below the turning frequency, there is $\mathrm{CLD}_{\mathrm{low}} < \mathrm{CLD}_{\mathrm{high}}$; once the frequency is higher than the turning frequency, $\mathrm{CLD}_{\mathrm{low}}$ will be larger than $\mathrm{CLD}_{\mathrm{high}}$. According to (31) and (32), the intersection is corresponding to the turning frequency. It is necessary to choose the suitable core material according to the equivalent frequency. It should be pointed that the conclusion above is deduced based on the experimental results in limited parameter space. More samples shall be examined to testify this empirical conclusion.

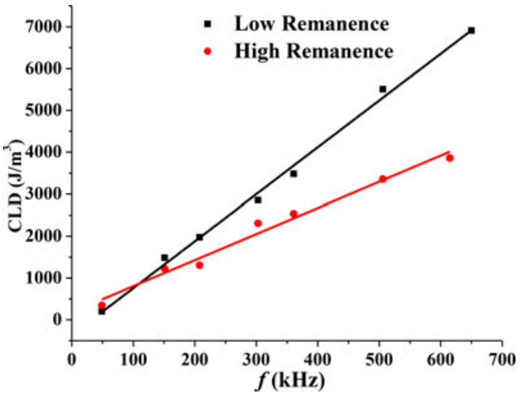

Fig. 19. CLD of FE-N cores at different equivalent frequencies.

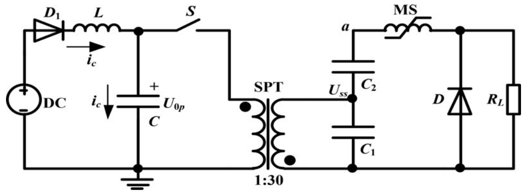

Fig. 20. Circuit schematic of the pulse generator.

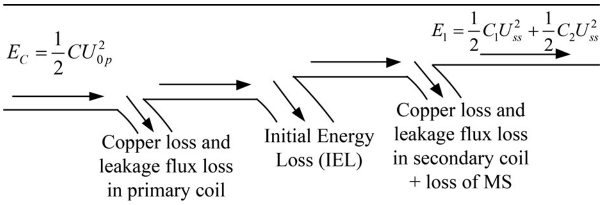

Fig. 21. Energy flow of the resonant charging circuit based on the SPT.

IV. Application of Results in an SPT Design

A repetitive nanosecond pulse generator based on the SPT and MS is designed and optimized. The circuit is similar to the one in [26] and shown in Fig. 20. Based on the test results in Section III, a flowchart for the design of the SPT is shown in Fig. 22. The results are listed in Table III.

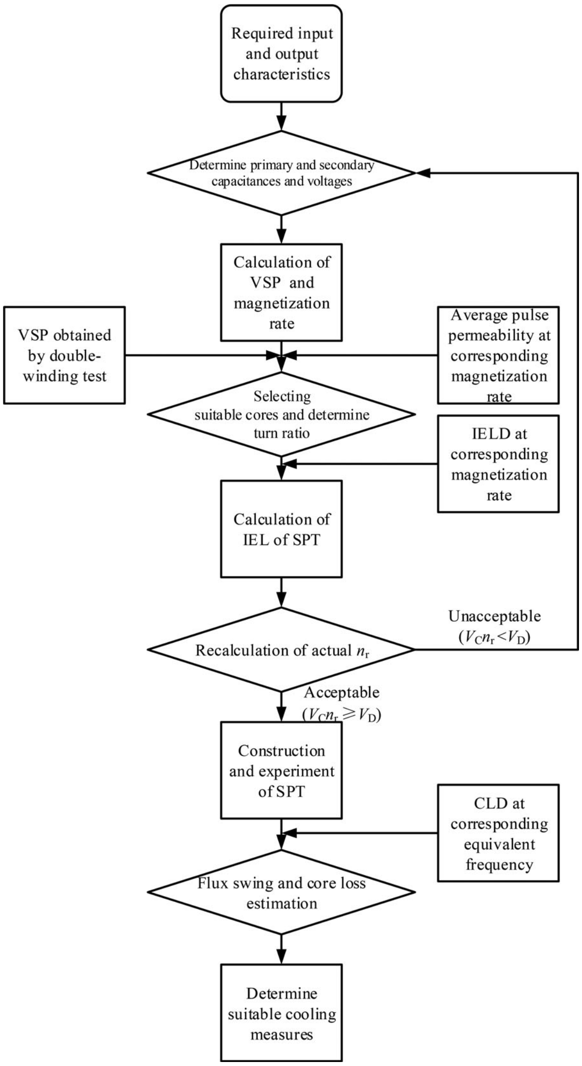

Fig. 22. Flowchart for the design of the SPT.

TABLE III
PARAMETERS OF THE SPT

	Parameters	Values
Initial parameters	C	1.336 μF
	$\mathrm{V_c}$	800 V
	$\mathrm{C_1}$ and $\mathrm{C_2}$	0.5 nF
	Desired peak voltage across $\mathrm{C_1}$ $\mathrm{V_D}$	25 kV
	Transformation ratio	30
	Ideal Resonant transformation ratio	30 × 1.5
	Maximum operation frequency $\mathrm{f_{PG}}$	5000 pps
Parameters for the construction of SPT	VSP of primary winding	1.2 kV·μs
	Magnetization rate	0.67 T/μs
	Remanence of the core	Low
	Number of the cores	3
	IELD	146.8 J/m^3
	IEL	0.045 J
	Actual n_{r} (calculation)	30 × 1.15
	Actual n_{r} (experiment)	30 × 1.10
	Average pulse permeability (0–0.8 T)	4250
	Primary winding	1 turn
	Secondary winding	30 turns
	Stray inductance in circuit	1.65 μH
Parameters for the core loss estimation	Oscillation duration	70 μs
	Typical waveform in one shoot	In Fig. 23
	Typical equivalent frequency	In Table IV
	$\mathrm{CL_{SPT}}$ in one shoot	$<$0.16 J
	P_{cL} (5000 pps)	$<$800 W

Most parameters are calculated based on further analysis considering the saturation of the MS. The magnetization rate of the SPT is estimated by (21). At 0.67 ($\sim$0.7) T/μs, the high-remanence FE-N core has a little bit lower IELD than that of the low-remanence one, as shown in Fig. 17. However, the core is demagnetized by the reverse discharge current, and no specialized demagnetization circuit is designed. If the high-remanace core is selected, accumulative magnetic bias of the core may occur and result in bad consistency of output pulses. So the low-remanence core is selected in order to keep the SPT working from the initial point of the *B–H* curve in the repetitive operation modes. The VSP of the SPT can be calculated as 1.2 kV·μs (converted to the primary side) [6]. In order to reduce the charging time, it is necessary to decrease the leakage inductance of the SPT. So the primary winding is chosen as one turn. It is also conducive to construct the SPT and keep enough insulation. The volume of the core can be calculated, and three above mentioned cores (outer radius $r_o = 55$ mm, inner radius $r_i = 30$ mm, and height $h = 20$ mm) are used [6]. The resonant charging process of C_1 and C_2 can be illustrated based on the equivalent Γ-type circuit of the pulse transformer [6]. In the duration of resonant charging, C_1 and C_2 are both charged to U_{ss} on condition that the MS saturates properly. U_{ss}/U_{0p} is usually higher than the winding ratio *n* because of the resonance of *CLC*. Therefore, resonant transformation ratio n_r is defined as

$$n_r = U_{ss}/U_{0p}. \tag{33}$$

The ideal resonant transformation ratio can be calculated according to the equivalent Γ-type circuit without considering the core loss [6]. However, as shown in Fig. 21, part of the energy in *C* is to be transferred into the IEL of the core, and it results in lower actual n_r than the ideal resonant transformation ratio.

The energy transferred from *C* to C_1 and C_2 can be recalculated by

$$E_C = E_{\mathrm{Cu}} + E_{\mathrm{air}} + E_{\mathrm{MS}} + E_1 + \mathrm{IEL} \tag{34}$$

where

$$E_C = \frac{1}{2} C U_{0p}^2 \tag{35}$$

$$E_1 = \frac{1}{2} C_1 U_{ss}^2 + \frac{1}{2} C_2 U_{ss}^2. \tag{36}$$

In the construction of the SPT, some measures are taken to make the wires as short as possible and the windings as tight as possible. In the design of the SPT, the cooper loss, leakage flux loss, and loss of the MS (which will be considered in the design of MS) are ignored. Once IEL is obtained by IELD, the actual n_r of the SPT can be recalculated in the design of SPT according to (33)–(36).

Single-shoot experiment is conducted after the SPT construction (the SPT prototype is shown in Fig. 23), and the core loss power of the SPT under repetitive operation condition is

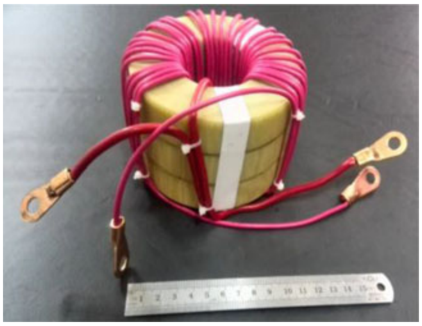

Fig. 23. SPT prototype.

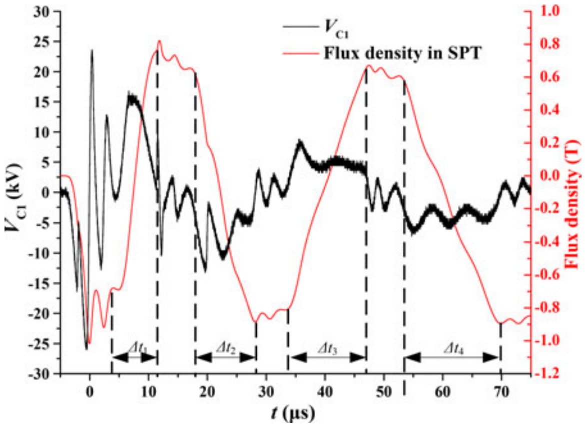

Fig. 24. Typical waveform of V_{c1} and flux swing of the SPT.

TABLE IV
EQUIVALENT FREQUENCIES OF FLUX SWING

Δt_n	Value (μs)	f_n (kHz)	CLD_n (J/m^3)	CL_n (J)
Δt_1	7.1	70.4	423	0.132
Δt_2	11.1	45.0	202	0.063
Δt_3	13.7	36.5	$<$202	$<$0.063
Δt_4	17.2	29.1	$<$202	$<$0.063

estimated. The typical waveform of U_{c1} and the flux swing of the SPT are shown in Fig. 24. U_{c1} has a perfect repeatability in each single shoot, but it is too complicated to be analyzed in detail. A simplification shall be made for the loss estimation. The equivalent frequency of the flux swing can be obtained by the definition of (30). Equivalent frequencies of the flux swing of the SPT in one shoot are listed in Table IV. Due to the fact that each interval corresponds to one branch of the hysteresis loop, the core loss energy of the cores of the SPT is calculated by

$$\mathrm{CL}_{\mathrm{SPT}} = 3\sum_{i=1}^{k} \mathrm{CL}_i \Big/ 2, \qquad n = 1, 2, 3\ldots \tag{37}$$

where *k* is the number of intervals obtained from Fig. 24. When $t > 70$ μs, it is believed that the magnitude of flux swing will approach zero, and the equivalent frequencies will be much lower than the first ones'. Therefore, the loss after 70 μs will be much lower. Besides, because not all of the IEL contributes to the temperature rise, IEL is not taken into account in the core loss estimation. The research on energy distribution of the IEL will be conducted in the future. Consequently, only the first four intervals are considered, and the loss power can be calculated by

$$P_{\mathrm{CL}} = \mathrm{CL}_{\mathrm{SPT}} \times f_{\mathrm{PG}} \tag{38}$$

where f_{PG} is the operation frequency of the pulse generator. If f_{PG} is 5 kHz, then P_{CL} will be less than 800 W. Suitable cooling measures (natural cooling, cooling fan, immersion in oil and so on) are to be determined based on the loss power estimation above and some widely used empirical formula. The design of the SPT in the pulse generator is an example of the application of the testing results. Although the magnetization rate and equivalent frequency above are relatively low, the design procedure and test results can be applied to other conditions. For example, if the U_{0p} is upgraded to 8 kV for higher output voltage, the magnetization rate will be 7 T/μs. It is convenient to redesign a SPT based on aforementioned procedures.

V. CONCLUSION

While prior work has investigated the loss density and permeability of nanocrystalline cores and other magnetic cores applied in power systems and power electronics, this paper has made a significant contribution analyzing pulse magnetic properties measurement and characterization of FE-N cores for high-voltage pulse magnetic applications.

1) The pulse magnetization characteristics under the single-winding test circuit include the space magnetization effect, and this leads calculation errors of the pulse permeability and saturated inductance. It is necessary to analyze the pulse magnetization characteristics of magnetic materials under the double-windings test circuit.
2) In pulsed power applications, two kinds of loss densities of the core, including the IEL density and CLD, can be tested under high magnetizing rates and high equivalent frequencies under the normal circuit. They can be easily used to guide the design of pulse magnetic components combining the proper calculation.

REFERENCES

[1] S. H. Kim and M. Ehshi, "Control and analysis of magnetic switch reset current in pulsed power systems," *IEEE Trans. Power Electron.*, vol. 29, no. 2, pp. 529–533, Feb. 2014.
[2] S. H. Kim, J. B. Park, S. D. Choi, Y. H. Kim, and M. Ehshi, "Optimal control method of magnetic switch used in high voltage power supply," *IEEE Trans. Power Electron.*, vol. 28, no. 3, pp. 1605–1071, Mar. 2013.
[3] S. Abuazoum, S. M. Wiggins, R. C. Issac, G. H. Welsh, G. Vieux, M. Ganciu, and D. A. Jaroszynski, "A high voltage pulsed power supply for capillary discharge waveguide applications," *Rev. Sci. Instrum.*, vol. 82, pp. 063505-1–063505-4, 2011.
[4] J. Choi, T. Namihira, T. Sakugawa, S. Katsuki, and H. Akiyama, "Loss characteristics of a magnetic core for pulsed power application," *IEEE Trans. Plasma Sci.*, vol. 35, no. 6, pp. 1791–1796, Dec. 2007.
[5] M. Watanabe, J. Kamiya, and T. Takayanagi, "Design and circuit simulation of a magnetic switching system for Kicker magnet power supply of 3 GeV RCS in J-PARC," *IEEE Trans. Appl. Supercond.*, vol. 20, no. 3, pp. 1681–1684, Jun. 2010.

[6] Y. Liu, X. Feng, and F. Lin, "Design and performance of a pulse transformer based on Fe-based nanocrystalline core," *Rev. Sci. Instrum.*, vol. 82, pp. 084703-1–084703-6, 2011.

[7] R. Burdt, R. D. Curry, K. F. Mcdonald, P. Melcher, R. Ness, and C. Huang, "Evaluation of nanocrystalline materials, amorphous metal alloys, and ferrites for magnetic pulse compression applications," *J. Appl. Phys.*, vol. 99, pp. 08D911-1–08D911-3, 2006.

[8] J. Choi, T. Namihira, and T. Sakugawa, "Simulation of 3-staged MPC using custom characteristics of magnetic cores," *IEEE Trans. Dielectr. Electr. Insul.*, vol. 14, no. 4, pp. 1025–1032, Aug. 2007.

[9] W. Shen, F. Wang, D. Boroyevich, and C. W. Tipton, "Loss characterization and calculation of nanocrystalline cores for high-frequency magnetics applications," *IEEE Trans. Power Electron.*, vol. 23, no. 1, pp. 475–484, Jan. 2008.

[10] R. Burdt and R. D. Curry, "Magnetic core test stand for energy loss and permeability measurement at a high constant magnetization rate and test for nanocrystalline and ferrite materials," *Rev. Sci. Instrum.*, vol. 79, pp. 094703-1–094703-6, 2008.

[11] F. Lin, Y. Liu, and X. Feng, " Study on a magnetic switch for pulsed power conditioning system," *IEEE Trans. Plasma Sci.*, vol. 40, no. 4, pp. 1183–1189, Apr. 2012.

[12] J. Muhlethaler, J. Biela, J. W. Kolar, and A. Ecklebe, "Improved core-loss calculation for components employed in power electronic systems," *IEEE Trans. Power Electron.*, vol. 27, no. 2, pp. 964–973, Feb. 2012.

[13] T. Hatakeyama and K. Onda, "Core loss estimation of various materials magnetized with symmetrical/asymmetrical rectangular voltage," *IEEE Trans. Power Electron.*, vol. 29, no. 12, pp. 6628–6635, Dec. 2014.

[14] Y. W. Choi, I. W. Jeong, G. H. Rim, H. S. Lee, E. P. Pavlov, C. S. Choi, M. H. Woo, and S. P. Lee, "Development of a magnetic pulse compression modulator for flue gas treatment," *IEEE Trans. Plasma Sci.*, vol. 30, no. 5, pp. 1632–1636, Oct. 2002.

[15] A. W. Molvik and A. Faltens, "Induction core alloys for heavy-ion inertial fusion-energy accelerators," *Phys. Rev. Spec. Topics-Accelerators Beams*, vol. 5, pp. 080401-1–080401-20, 2002.

[16] M. Mu, Q. Li, D. J. Gilham, F. C. Lee, and K. D. T. Ngo, "New core loss measurement method for high-frequency magnetic materials," *IEEE Trans. Power Electron.*, vol. 29, no. 8, pp. 4374–4381, Aug. 2014.

[17] C. H. Smith, "Applications of amorphous magnetic materials at very high magnetization rates," *J. Appl. Phys.*, vol. 67, no. 9, pp. 5556–5562, May 1990.

[18] R. H. Wang, *Design of Pulse Transformers*. Beijing, China: Science Press, 1996, pp. 58–66.

[19] A. F. Witulski, "Introduction to modeling of transformers and coupled inductors," *IEEE Trans. Power Electron.*, vol. 10, no. 3, pp. 349–357, May 1995.

[20] G. W. Ludwig and S. A. E. Hamamsy, "Coupled inductance and reluctance models of magnetic components," *IEEE Trans. Power Electron.*, vol. 6, no. 2, pp. 240–250, Apr. 1991.

[21] A. V. Radun, "Development of dynamic magnetic circuit models including iron saturation and losses," *IEEE Trans. Magn.*, vol. 50, no. 5, pp. 1–10, May 2014.

[22] A. Davoudi, P. L. Chapman, J. Jatskevich, and A. Khaligh, "Reduced-order modeling of high-fidelity magnetic equivalent circuits," *IEEE Trans. Power Electron.*, vol. 24, no. 12, pp. 2847–2855, Dec. 2009.

[23] A. Davoudi, P. L. Chapman, and J. Jatskevich, "Reduced-order dynamic modeling of multiple-winding power electronic magnetic components," *IEEE Trans. Power Electron.*, vol. 27, no. 5, pp. 2220–2226, May 2012.

[24] Y. Han, G. Cheung, A. Li, C. R. Sullivan, and D. J. Perreault, "Evaluation of magnetic materials for very high frequency power applications," *IEEE Trans. Power Electron.*, vol. 27, no. 1, pp. 425–435, Jan. 2012.

[25] Y. Yang and Z. Li, "Effect of composite magnetic annealing in amorphous alloys," *IEEE Trans. Magn.*, vol. 18, no. 6, pp. 1397–1399, Nov. 1982.

[26] A. Pokryvailo, M. Wolf, Y. Yankelevich, S. Wald, L. R. Grabowski, E. M. Veldhuizen, W. R. Rutgers, M. Reiser, B. Glocker, T. Eckhardt, P. Kempenaers, and A. Wellman, "High-power pulsed corona for treatment of pollutants in heterogeneous media," *IEEE Trans. Plasma Sci.*, vol. 34, no. 5, pp. 1731–1743, Oct. 2006.

Yi Liu (S'10–M'14) was born in Hunan, China, in 1985. He received the B.S. degree in electrical engineering from Wuhan University, Wuhan, China, in 2008, and the Ph.D. degree in lectrical and electronic engineering from the Huazhong University of Science and Technology (HUST), Wuhan, in 2013.

He is currently a Lecturer in the School of Electrical and Electronic Engineering, HUST. His research interests include high-voltage engineering and pulsed power technology.

Yibo Han was born in Wuhan, Hubei, China, in 1991. He received the B.S. degree in electrical engineering and automation from Xi'an Jiaotong University, Xi'an, China, in 2013. He is currently working toward the M.S. degree in electrical engineering in the Department of High-Voltage Engineering from the Huazhong University of Science and Technology, Wuhan.

His research interests include high-voltage engineering and pulsed power technology.

Siwei Liu was born in Hubei, China, in 1992. He received the B.S. degree in electrical engineering and automation from the Huazhong University of Science and Technology (HUST) in 2014, where he is currently working toward the M.S. degree in electrical engineering in the Department of High-Voltage Engineering.

His research interests include high-voltage engineering and pulsed power technology.

Fuchang Lin (M'10) was born in Zhejiang, China, in 1969. He received the Ph.D. degree in electrical and electronic engineering from the Huazhong University of Science and Technology (HUST), Wuhan, China, in 1996.

He is currently a Professor with the School of Electrical and Electronic Engineering, HUST, where he has been working on pulsed power technology and high-voltage engineering.

Dr. Lin is a Member of the Chinese Society for Electrical Engineering.